JOURNAL OF MATERIALS SCIENCE 27 (1992) 3539–3551

Production of Al–(12–25) wt % Si alloys by rapid solidification: melt spinning versus centrifugal atomization

P. TODESCHINI
Centre de Recherche Nucléaire, Paris, France

G. CHAMPIER
Laboratoire de Physique du Solide, Ecole des Mines, Parc de Sauropt, 54042 Nancy Cedex, France

F. H. SAMUEL
Département des Sciences Appliquées, Université du Québec à Chicoutimi, Chicoutimi, Québec, Canada G7H 2B1

Al–Si–x (x = Cu, Mg, Ni, Co or Sr) alloys with Si content in the range 12–25 wt % were quenched from the liquid state using two methods: melt spinning and centrifugal atomization. The powders obtained were degassed followed by hot extrusion. Effects of chemical composition, quenching conditions, hot extrusion and heat treatment on the variation in the microstructure were examined. The present results show the necessary conditions for supersaturated solid solution, and those required for mechanism of solute trapping by moving the solid/liquid interface. Also, the mechanical properties of the products obtained were evaluated. It is observed that melt spun ribbons with Si concentrations of more than 12% possess high yield strength with low ductility. These materials undergo softening on ageing at temperatures above 150 °C. The properties of extruded alloy powders are markedly improved as compared to those made by ingot metallurgy. This effect is mainly due to the silicon particle refinement brought about by rapid solidification with cooling rates higher than 10^5 K s^{-1}.

1. Introduction

The rapid solidification technique, with cooling rates $> 10^3$ K s^{-1}, allows the preparation of alloys with microstructures very different from those produced by classical foundry. These microstructures are associated with physical properties that have a number of important characteristics. In the case of crystalline microstructure, crystals of fine primary phase, supersaturated solid solution and an improved chemical homogeneity have been reported [1–5].

The present study dealt with Al–Si alloys containing Si less than 25 wt %. These alloys are characterized by their excellent castability and less rejection after solidification. They represent the base for most foundry aluminium alloys. Also, they offer good wear resistance, low thermal expansion and exceptional properties for pistons, engine blocks and different parts of thermal motors.

The work undertaken aimed at investigating the effect of melt quench on improving the mechanical properties of foundry aluminium alloys for the automotive industries. Also, one of the major objectives of the work was to produce massive pieces by the compacting of powders produced by centrifugal atomization.

2. Experimental procedure

Binary Al–Si (12, 17, 20 and 25 wt %) alloys were prepared from high purity metals under an inert atmosphere of argon. The addition of Cu, Ni, Mg, Co and Sr as ternary alloying elements was limited to Al–12 wt % Si binary alloy for centrifugal atomization. The chemical analysis of these alloys is given in Table I.

All alloys were spun into ribbons by conventional melt spinning using a Cu–2% Cr wheel (27 cm in diameter) as the rotating chill substrate. The melt spinning was done in a chamber under H_2 atmosphere.

Al–12 wt % Si alloys was atomized into powders by the centrifugal method. Ingots of 400 g were melted in a graphite crucible having an orifice of 1 mm diameter and coated with a thick layer of boron nitride refractory. The atomizing chamber was evacuated and filled

TABLE I Chemical composition of Al–Si–x powders

Alloy designation	Element (wt %)						
	Si	Cu	Mg	Ni	Co	Sr	Fe
Al–12% Si	13.2	–	–	–	–	–	0.05
Al–Si–Cu	12.4	1.9	–	–	–	–	–
Al–Si–Mg	12.4	–	2.8	–	–	–	–
Al–Si–Ni	12.3	–	–	1.1	–	–	–
Al–Si–Co	12.4	–	–	–	0.5	–	–
Al–Si–Sr	12.3	–	–	–	–	0.07	0.10

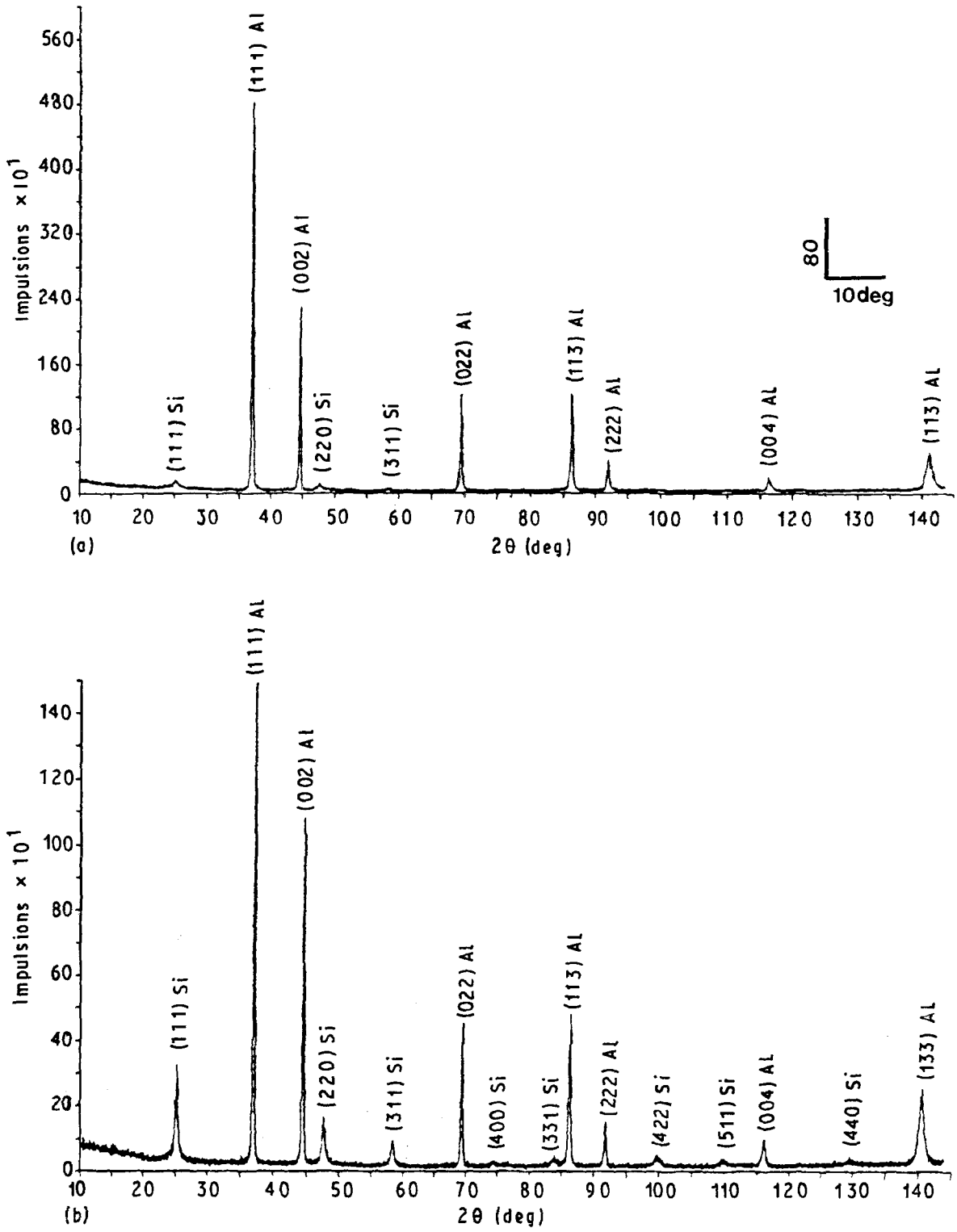

Figure 1 X-ray diffraction patterns obtained from as-melt spun: (a) Al–12 wt % Si and (b) Al–25 wt % Si.

with H_2 up to 1×10^5 Pa. The liquid metal was ejected on to a rotating atomizer (a 43 mm diameter graphite disc, coated with boron nitride, heated to 800 °C, and running at 27 300 rev min^{-1}) with a helium overpressure of 0.4×10^5 Pa. At the end of atomization, the temperature of the rotating atomizer had fallen between 600 and 650 °C.

The atomized powders were collected in aluminium cans (2 mm thick, and subjected to degassing for 24 h at 200 °C under vacuum (10^{-4} Pa). These cans, thereafter, were hot extruded into rods at 250–300 °C, with an extrusion ratio of 28:1. The inner diameter of the compacted rods was about 9 mm.

Thin foils for transmission electron microscopy (TEM) were prepared from the spun ribbons by electropolishing in an (80% methanol + 20% perchloric acid) electrolyte, followed by ionic bombardment (argon ions at 5 keV).

Loose powders were embedded in nickel discs using an electrolytic method described by Kelly and Van der Sande [6]. Thin foils were prepared from these discs following the above mentioned technique.

Specimens for tensile tests were machined either from the spun ribbons (5 mm gauge, 1 mm width and 40 μm thickness) using a special device or from the extruded rods (20 mm gauge and 4 mm diameter).

X-ray diffraction (XRD) was carried out using CoK_α radiation (= 0.1786 nm), on ribbons or loose powders pasted on glass plates using an amorphous glue.

3. Results and discussion

3.1. Melt spun ribbons

3.1.1. X-ray analysis

Fig. 1 shows the diffractograms obtained from Al–12% and 25% Si solidified at 10^6 K s^{-1}. Increasing the Si content resulted in increasing the number of Si peaks without the formation of any other intermediate phases [7, 8].

Table II shows the average concentration of Si in α-Al as a function of Si content in the alloy. The average thickness of the ribbon was kept constant, of the order 40 μm and the superheat in the range 25–55 K. The values obtained for 20 and 25% Si were not very significant. This indicates that there was a supersaturation breakdown as evident from the value of the α-Al lattice parameter, 0.4049 versus 0.40468 nm which represents the limit for the thermodynamic solubility. Thus, it is concluded that the concentration of Si in α-Al increases with the Si content, reaching a maximum value of 4.2 at % for Al–17% Si. Thereafter, there is an abrupt decrease in Si concentration reaching almost 0% when the Si content is 20% or more.

Table III shows the average concentration of Si in α-Al as a function of melt superheat. These results reveal that there is an inverse proportion between the concentration of Si in α-Al and Si content.

Fig. 2 demonstrates the variation in lattice parameter of α-Al as a function of Si content, for different ribbon thicknesses and melt superheats. As expected, increasing the Si content up to 17% leads to a linear decrease in the value of α. This relation can be expressed as:

$$\alpha = 0.40485 - 0.26 \times 10^{-4}(\text{Si at \%}) \quad (1)$$

The fact that the value of α = 0.2051 nm for 20% Si (α = 0.40495 nm for pure aluminium) is explicable in terms of auto-ageing immediately after solidification and during cooling to room temperature. Similar results have been reported by Mittemeijer *et al.* [9], who found that α = 0.4051 nm after ageing Al–22.4% Si melt spun ribbons at 172 °C.

TABLE II Effect of alloy composition on the average concentration of Si in α-Al phase

Composition	12% Si	17% Si	20% Si	25% Si
Thickness (μm)	40	40	38	40
Superheat (K)	50	50	50	50
α-Al (nm)	0.4045	0.4043	0.4053	0.4051
Si concentration in α (at %)	2.6 ± 0.3	3.8 ± 0.3	0	0

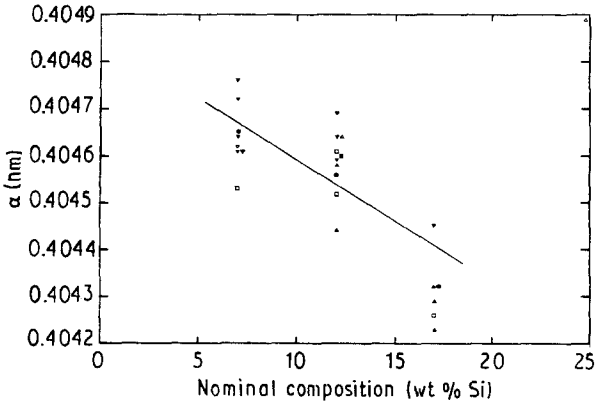

Figure 2 Variation in the value of the lattice parameter α as a function of Si content.

3.1.2. Microstructure

Fig. 3a is the cross-section microstructure of as-melt spun Al–12% Si, comprising of two zones marked A and B. Zone A, which is close to the wheel, is characterized by its resistance to chemical etching (white zone). The thickness of this zone is about 10 μm. Zone B, gas side, is about 30 μm thick. The microstructure of this zone consists of equiaxed α dendrites or rosettes surrounded by dark areas rich in silicon. The size of the α crystals varies from 4 (near the wheel side) to 3 μm (near the gas side). The average dendrite arm spacing is of the order 0.5–0.7 μm. In some cases, a columnar structure inclined at 80 degs with respect to the longitudinal direction of the ribbon was observed. The average diameter of columnar grains was about 0.4 μm, as viewed by optical microscopy. The thickness of the white zone (A) decreased progressively as the Si content increased (Fig. 3b). As can be seen in this microstructure, crystals of pure silicon are clearly visible, whereas α-Al occurs more or less as equiaxed crystals through the entire cross-section.

In order to study the effect of the presence of the white zone on the value of the lattice parameter α, the

TABLE III Effect of melt superheat on the concentration of Si in α-Al

Composition	12% Si			17% Si		
Thickness (μm)	35	35	33	30	30	35
Melt Superheat (K)	20	30	140	20	30	150
α-Parameter (nm)	0.4046	0.4044	0.4047	0.4043	0.4042	0.4043
Concentration of Si in α-Al (wt %)	2.1 ± 0.3	3.2 ± 0.3	1.5 ± 0.33	3.8 ± 0.3	4.4 ± 0.3	3.8 ± 0.3

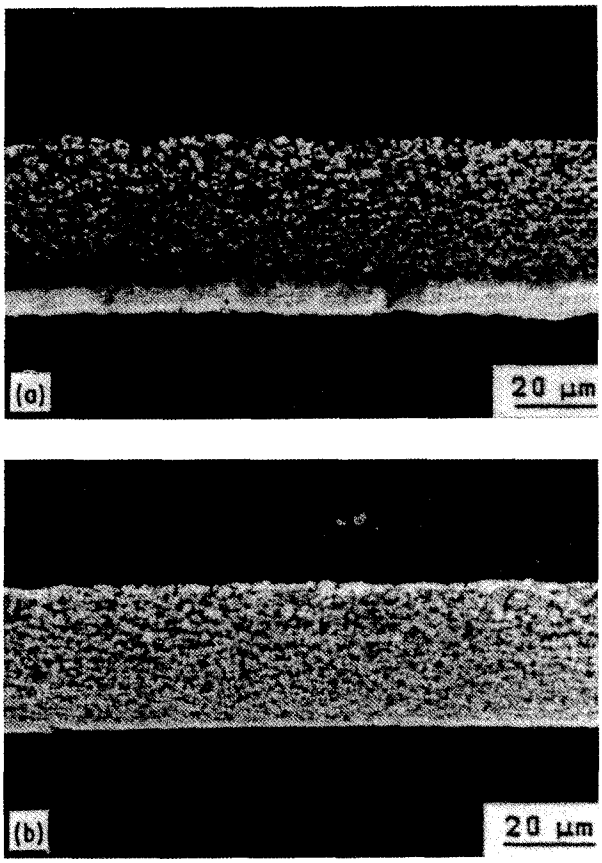

Figure 3 Optical microstructure of as melt-spun (a) Al–12% Si, 55 μm thick and (b) Al–25% Si, 37 μm thick. In (a) the white line is zone A and the region immediately above is zone B.

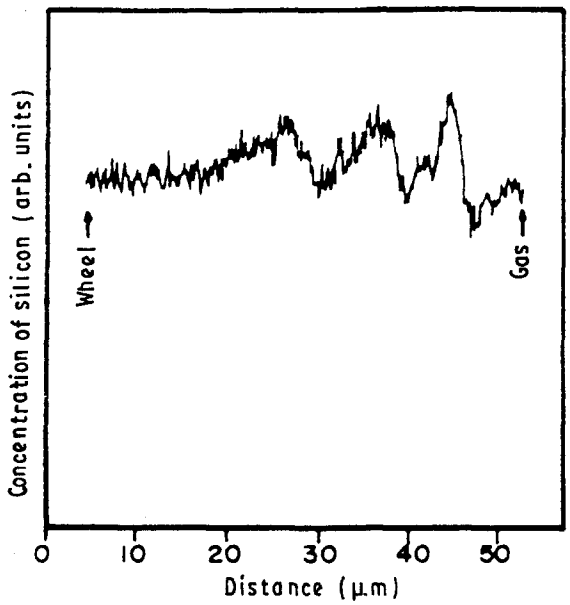

Figure 4 Profile of the concentration of Si (in arbitrary units) through the cross-section of Al–12 % Si melt spun ribbon.

white zone shown in Fig. 3a (8 μm thick) was exposed to X-rays. Thereafter, 20 μm were removed from the gas side and the white zone was re-exposed to X-rays. The α values obtained were 0.40442 and 0.40446, respectively, (see Table II for the average values). This result allows us to assume that supersaturation in zone A is much higher than that in zone B. However, the presence of zone A has a relatively weak effect on the α value since it only changes from 0.40446 to 0.40442.

The concentration of Si through the cross-section was studied by electron microprobe analyser using the ribbons shown in Fig. 3a. The results are displayed in Fig. 4. As can be seen, there is no change in concentration for the first 15 μm (measured from the wheel side). Thereafter, there is a significant fluctuation in the homogeneity of the matrix as the electron beam approaches the gas side.

Thin foils prepared from the as-melt spun ribbons were examined using a 200 kV transmission electron microscope. The white zone presented in Fig. 3a was found to consist of two types of α-Al grains. The first type is an equiaxed grain structure, where the grains are separated by high angle boundaries. The possible Si/α-Al orientation relationships, as could be fixed from the corresponding electron diffraction patterns shown in Fig. 5a, are

$$(1\,0\,0)_{Si}//(1\,0\,0)_{Al}$$

$$(0\,1\,0)_{Si}//(1\,0\,0)_{Al}$$

The main characteristic feature of this structure is the homogeneous distribution of Si within the grains, Fig. 5b. Another type of granular microstructure representing an area very close to the wheel side, is shown in Fig. 6. This microstructure consists of high angle fine grains ≈ 0.2–0.8 μm. Within these grains, circular microdomains are observed. Ozawa and Kimura [10] have proposed that the presence of these microdomains is due to the pile-up of vacancies that act as preferential nucleation sites for Si particles. Si clusters in the neighbourhood of such vacancies result in the image shown in Fig. 6.

Fig. 7a represents a granular microstructure from another area close to the wheel side. Within their interiors a cellular structure could be viewed, Fig. 7b. Based on several photomicrographs similar to Fig. 7a, the average diameter of these cells is about 60 μm separated by an intercellular distance of 90 μm. The corresponding electron diffraction pattern of Fig. 6a revealed the presence of three Si rings: (1 1 1), (2 2 0) and (4 0 0). Fig. 6 is imaged on the diffracted ring (1 1 1). In this figure fine light spots about 1 nm diameter can be seen surrounded by a certain type of phase contrast. This phase may have occurred by crystallization of an amorphous phase during the course of cooling.

A classical cellular columnar structure was the main structure viewed in areas close to the centre of the ribbon. An example is shown in Fig. 8a, where fine cells of the order of 0.1–0.2 μm are seen along with coarse Si particles in the intercellular spaces, Fig. 8b.

The structure corresponding to the gas side was, in general, either equiaxed dendrites or rosettes, Fig. 9a. A dark field micrograph imaged on a Si diffracted spot shows the distribution of Si in the interdendritic space, Fig. 9b, distributed in the form of domains, each with 1 nm diameter.

The as-melt spun ribbons were aged isochronally for 3 h at 150, 200 and 250 °C. For zone A (or wheel

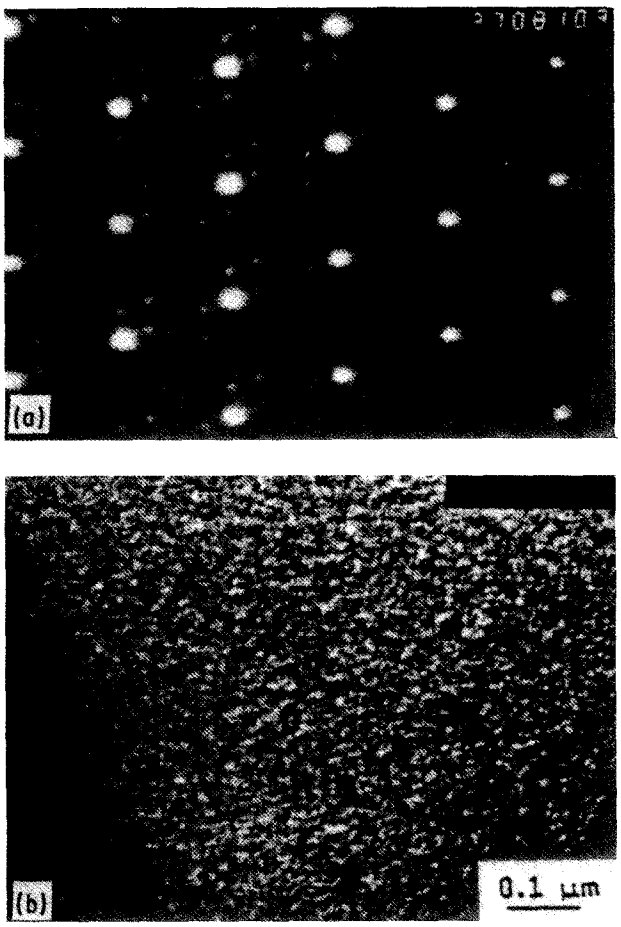

Figure 5 TEM micrographs obtained from white zone shown in Fig. 3a (a) electro diffraction pattern and (b) a dark field micrograph imaged on a Si diffracted spot.

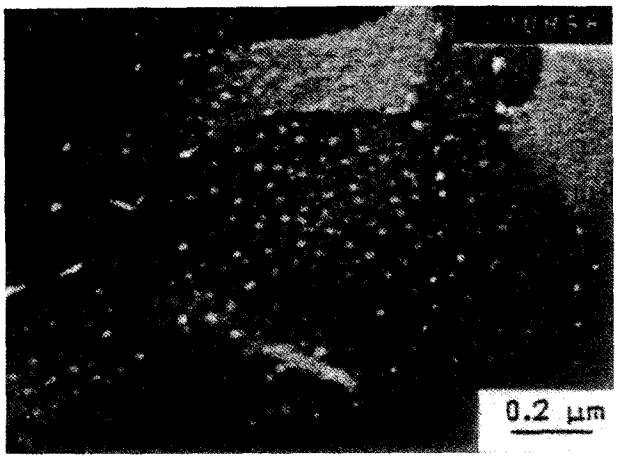

Figure 6 Dark field micrograph obtained from the white zone shown in Fig. 3a.

side, e.g. Fig. 3a), the size of the Si precipitates did not exceed 40 nm. Increasing the temperature (*in situ*) to 250 °C resulted in an increase of the Si particle size to around 100 nm. For zone B, the as-solidified structure was visible up to 200 °C. At 150 °C, fine interdendritic Si precipitates with an $\{1\,0\,0\}_{Si}//\{1\,0\,0\}_{Al}$ orientation relationship were noted. These precipitates were either in the form of needles (0.7 μm long and 5 nm diameter) or tetrahedrons ($\approx$ 70 nm), Fig. 10a. At 200 °C, the size of these precipitates increased to 0.3 μm length and 10 nm diameter for the former structure, and to 0.2 μm for the latter. At 250 °C, the as-solidified structure was no longer visible. Platelet-like Si particles, having the same orientation relationship with the matrix as above, represented the majority of precipitates viewed at this temperature. Their sizes ranged between 0.35 and 0.6 μm, Fig. 10b.

It is well established that the relationship between a characteristic size of microstructure and cooling rate is governed by the following relation:

$$d = A(T)^n \qquad (2)$$

where A and n are constants. Armstrong and Jones [11], and Matyja *et al.* [12] proposed $n = -1/3$ and $A = 47\ \mu m\, s^{1/3}\, K^{-1/3}$ for Al–11 at % Si. For the present Al–12 wt % Si, the measured dendrite arm spacing is about 0.6 μm. Thus, the expected cooling rate should be of the order $5 \times 10^5\ K\, s^{-1}$, for the gas side. For the wheel side, using $d = 0.09$ μm yields a cooling rate of about $7 \times 10^9\ K\, s^{-1}$, which is very close to that required for an amorphous structure.

Thermal models as proposed by Clyne [13], however, show that the above mentioned relation is inapplicable for the wheel side. According to him, the motion of the solidification front is accompanied by strong recalescence. Thus, it is more reliable to consider the solid/liquid interface velocity (V) rather than the cooling rate. For binary systems, the knowledge of the thermal gradient in the liquid is very important

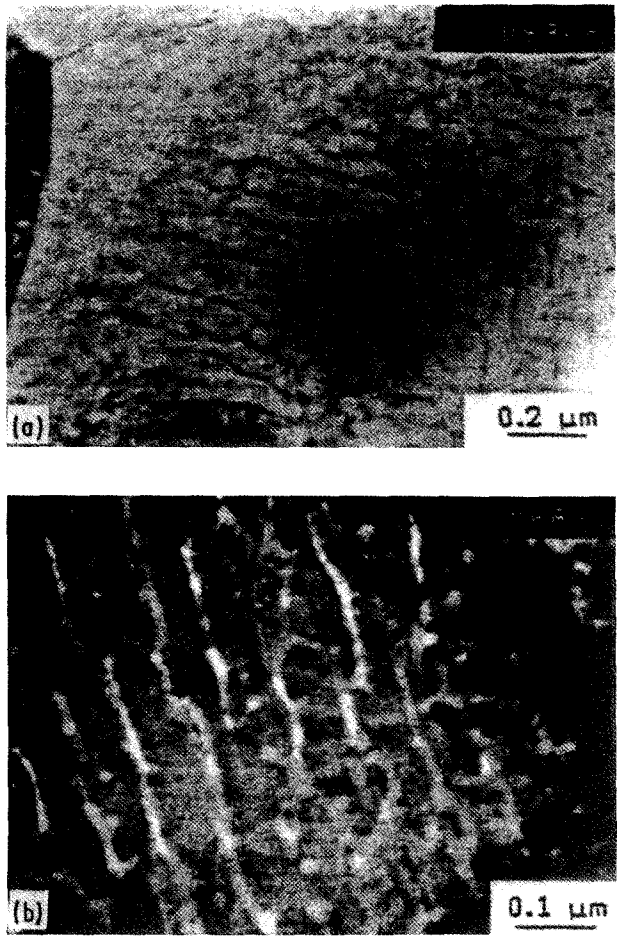

Figure 7 TEM micrographs taken from an area in immediate vicinity of the wheel side (Al–12% Si) (a) bright field (b) dark field.

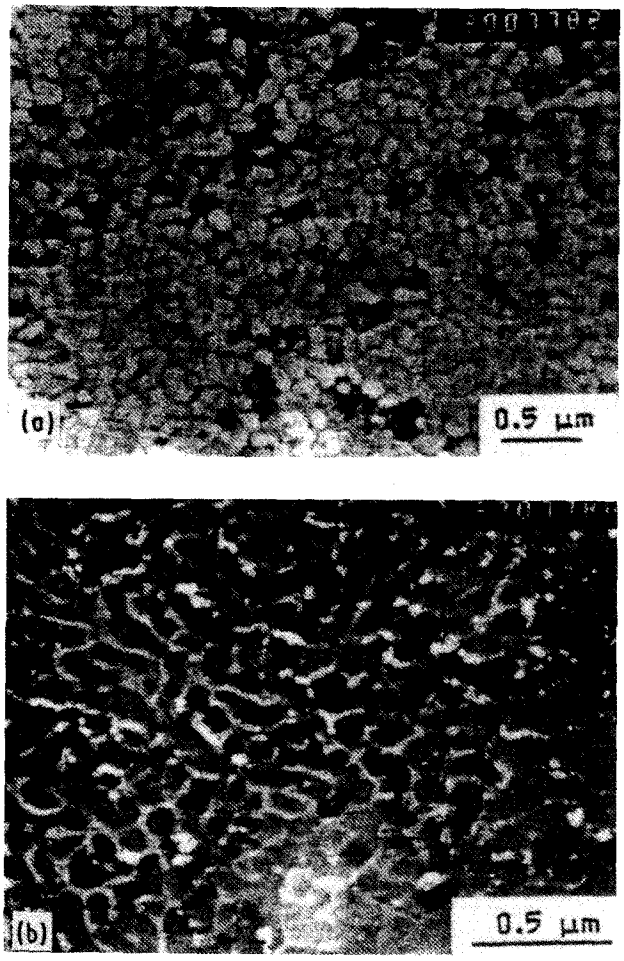

Figure 8 TEM micrographs taken from an area close to the ribbon centre (Al–12% Si) (a) bright field (b) dark field.

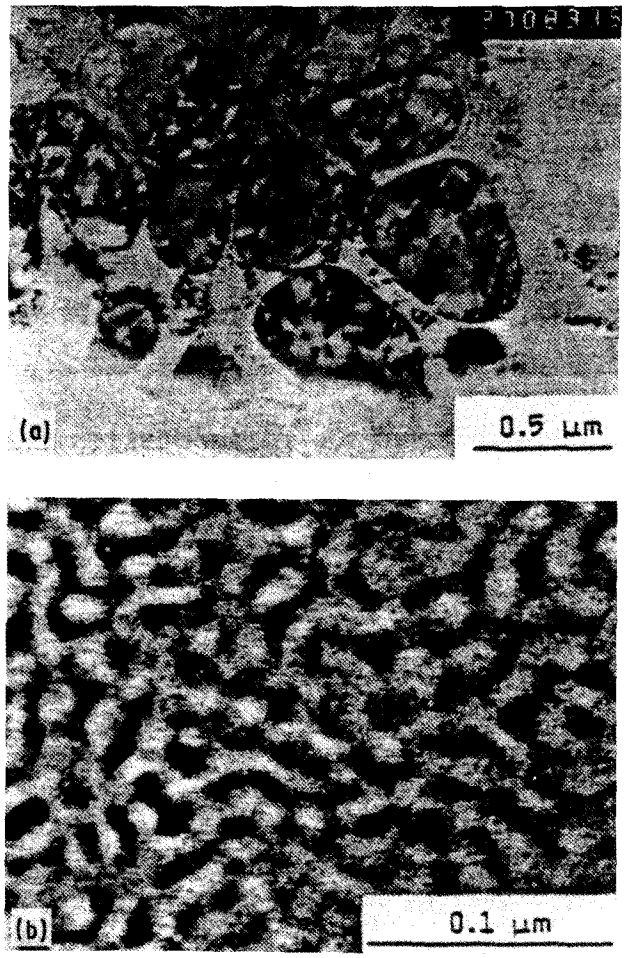

Figure 9 TEM micrographs taken from an area close to gas side (Al–12% Si) (a) bright field (b) dark field.

since this parameter controls the stability of the moving solid/liquid interface (the local time of solidification governs the maturation of the structure through the transport phenomenon in the liquid state).

According to a theory [14, 15], for a specific alloy composition there is a certain solid/liquid interface velocity that controls the absolute stability of the interface. Fig. 11 illustrates the conditions required for the stability of the moving interface for the present Al–Si alloys, as obtained from this theory and using the equation

$$V = (1 - k)mC_0D/k^2T_m\Gamma \quad (3)$$

where k is the partition coefficient, m is the slope of the liquidus line (K per wt %), C_0 is the nominal alloy composition (wt %), D is the diffusion coefficient of Si in liquid aluminium ($m^2 s^{-1}$), Γ is the solid/liquid interface energy ($J m^{-2}$), and T_m is the fusion temperature of pure metal (K).

In the present case, $m = 7$ K per wt %, $C_0 = 12$ wt %, $T_m = 933$ K, $K = 0.14$, $D = 5 \times 10^{-9} m^2 s^{-1}$ and $\Gamma = 1.2 \times 10^{-10} J m^{-2}$. Applying these values in Equation 3 yields $V = 200 m s^{-1}$, which does not have any physical significance. Thus, it is not the stabilization of the solid/liquid interface by the surface tension with the partition coefficient under thermodynamic equilibrium that leads to the formation of α-Al grains with no segregation observed in the layer in the immediate vicinity of the wheel.

It should also be noted that if there is no solute rejection during solidification, the partition coefficient, k, will approach unity, i.e. $V = 0$. Aziz [16] has reported the variation of the parameter k at the critical interfacial velocity V, given by the expression

$$V = D/\lambda \quad (4)$$

where λ is the distance between two successive atomic layers. For the present alloy, $V = 2 m s^{-1}$. Thus a sensible diminution of k could take place at $V = 2 m s^{-1}$ which, consequently, will drastically affect the value of V in Equation 3. Based on this, solute trapping in the solid is probably the physical phenomenon that explains the formation of planar grains with no solute segregation.

If zone A corresponds to columnar growth of the crystals of α-Al, the microstructure of zone B is a result of the nucleation of α-Al in the liquid aluminium. Clyne [13] arrived at a numerical model of thermal phenomena that occurred during melt-quench of pure aluminium using a copper wheel. Two successive phases can be developed, depending on the thermal history. In this case, an adiabatic solidification, the velocity of the moving solid/liquid interface is such that there is no heat exchange between the ribbon and cooling substrate to avoid the recalescence. This is

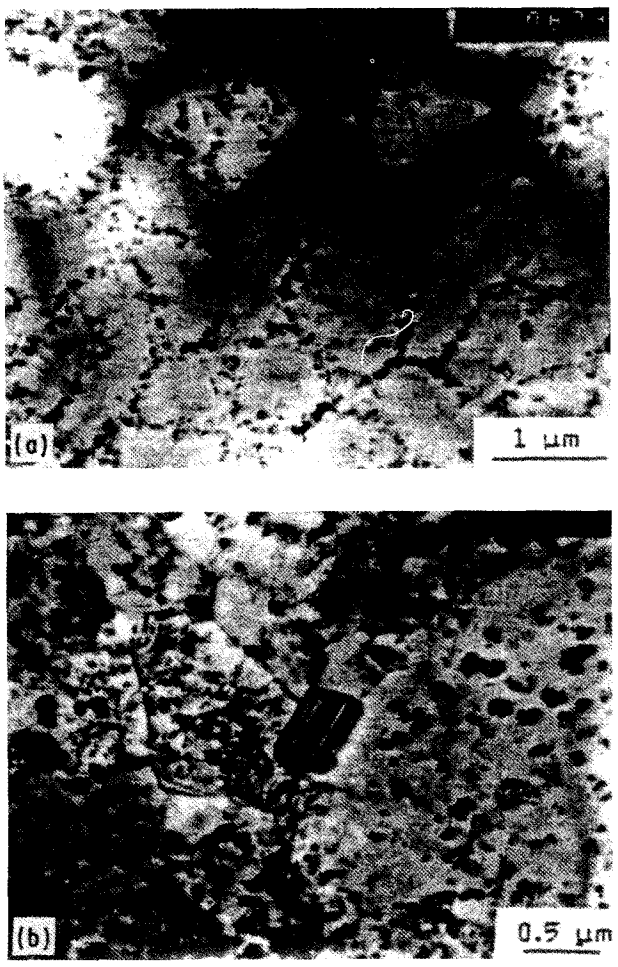

Figure 10 TEM micrographs of Al–17% Si aged 3 h at (a) 150 °C, bright field and (b) 250 °C, bright field.

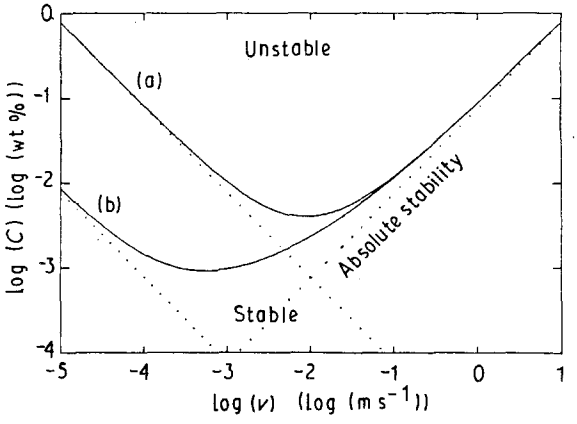

Figure 11 Concentration–interface velocity relationship for Al–Si system for two thermal gradients: (a) $G_L = 10^5$ K m^{-1} and $G_L = 10^3$ K m^{-1}.

followed by isothermal solidification that is controlled by the heat exchange between the ribbon and substrate. The interface velocity of a permanent regime is given by

$$V = q/(H - H_{sf}) \quad (5)$$

where q is the thermal flux towards the substrate, H is the alloy enthalpy, H_{sf} is the enthalpy of solid alloy at the fusion temperature.

For the present Al–12 wt % Si, the velocity is about 0.3 m s^{-1} for $H = 10^6$ W m^2 K^{-1} and the temperature interval between the ribbon and substrate, about 300 K.

In order to obtain an homogeneous microstructure over the entire thickness of the ribbon, the recalescence should be limited by the external heat transfer. For the Newtonian regime, the necessary condition is that the Mehrabian number, M_e, should not exceed unity

$$M_e = \frac{B(H - H_{sf})}{H} \quad (6)$$

$$B = \frac{V}{(T - T_f)} \quad (7)$$

where T is the alloy temperature and T_f is the alloy fusion temperature.

3.1.3. Mechanical properties

Microhardness values measured at the ribbon centre, using a load of 10 g are shown in Table IV. Increasing the silicon content resulted in a linear increase in the ribbon hardness, 0.7 GPa, up to 20% Si. Beyond this value and because of saturation, the hardness did not increase on increasing the silicon up to 25%.

Table V displays the change in hardness on ageing at 150, 200 and 250 °C. At 150 °C, there is a slow and gradual softening. However, this is not the case at 200 or 250 °C where a drastic decrease in the hardness is clearly observed after 2 h, followed by a steady state. These results are in good correlation with the observations made on the microstructure as reported in the previous section.

A few tensile tests were performed on flat specimens machined from the ribbons, 10 mm long and 1 mm gauge length. The obtained values of ultimate tensile strength are reported in Table IV. It is interesting to note Al–17% Si melt-quench attained a strength comparable to those obtained from high resistance aluminium alloys e.g., alloy 7075 T6, $\sigma_R = 572$ MPa.

3.2. Centrifugally atomized powders

3.2.1. X-ray analysis

The X-ray diffraction of Al–Si–Co and Al–Si–Sr powders revealed only α and Si phases. The addition of Cu to Al–Si powders resulted in the appearance of 19 peaks, corresponding to Al_2Cu (θ) phase. With Ni, two peaks at 0.1599 and 0.3022 nm corresponding to (1 0 1) and (1 3 1) reflections of Al_3Ni phase were seen,

TABLE IV Hardness and ultimate tensile strength ($\varepsilon \approx 10^{-3}$ s^{-1}) of as-melt spun ribbons

Si %	$H_{v0.01}$ (GPa)	σ_R (MPa)	
		Without machining	Machined
12	1.4	330	445
17	1.8	450	570
20	2.0	–	–
75	2.0	–	–

TABLE V Microhardness values (GPa) measured at the ribbon centre of Al–12% Si and Al–17% Si alloys aged at 150, 200 and 250 °C for various ageing times

Alloy composition	Ageing temperature (°C)	Ageing time (h)							
		0	1	2	3	4	5	6	7
Al–12% Si	150	1.38	1.35	1.33	1.30	1.26	1.23	1.19	1.17
	200	1.39	1.33	1.05	0.88	0.83	0.83	0.83	0.83
	250	1.38	0.86	0.77	0.70	0.68	0.66	0.63	0.62
Al–17% Si	150	1.72	1.69	1.66	1.63	1.61	1.58	1.52	1.50
	200	1.73	1.74	1.55	1.27	1.26	1.26	1.26	1.26
	250	1.72	0.91	0.90	0.90	0.90	0.89	0.89	0.89

Fig. 12d. There were very weak reflections that could not be indexed on the basis of ASTM standard diffraction patterns.

For the Al–Si–Mg powders, the X-ray diffraction pattern, Fig. 13, revealed the presence of two peaks due to Mg_2Si with 12 peaks of significant intensity. These peaks could not be indexed either, on the basis of ASTM standard published data for Al–Si–Mg rapidly solidified alloys [17–19]. It is thus concluded that the present system contains at least one meta-stable phase. These powders were aged under argon for 24 h at 200 and 250 °C. At 200 °C, these peaks are still visible, Fig. 13a. Two more peaks, at 0.259 and 0.334 nm, could be detected. It is believed that these peaks belong to the meta-stable phase. At this temperature, also, the intensity of the Mg_2Si and Si peak were noticeably increased. At 250 °C, however, all peaks of the meta-stable phase disappeared, Fig. 13b. The positions of these peaks are given in Table VI.

X-ray diffraction patterns obtained after hot extrusion revealed the presence of the same phases reported for loose powders along with characteristic reflections from Al_2Cu, Mg_2Si and Al_3Ni phases. A significant increase in the intensity of the $(0\,1\,1)_\alpha$ peak was also observed, with a remarkable decrease in the intensity of the $(1\,1\,1)_\alpha$ peak. As these diffractions were produced from specimens where the surface exposed to the X-rays was parallel to the extrusion direction, it is reasonable to conclude that the deformation texture is of $\langle 1\,1\,1 \rangle$ type [20]. The effect of texture was more pronounced in the Al–Si–Cu and Al–Si–Mg alloys.

3.2.2. Microstructure

Optical microstructures of polished sections prepared from as-melt quenched loose powders are shown in Fig. 14. Two main observations could be made:

1. Fine microstructure consisting of α-Al crystals possessing the form of dendrites or cells. As the diameter of the powder particles decreased, the secondary dendrite arms tended to disappear and be completely replaced by a cellular structure.

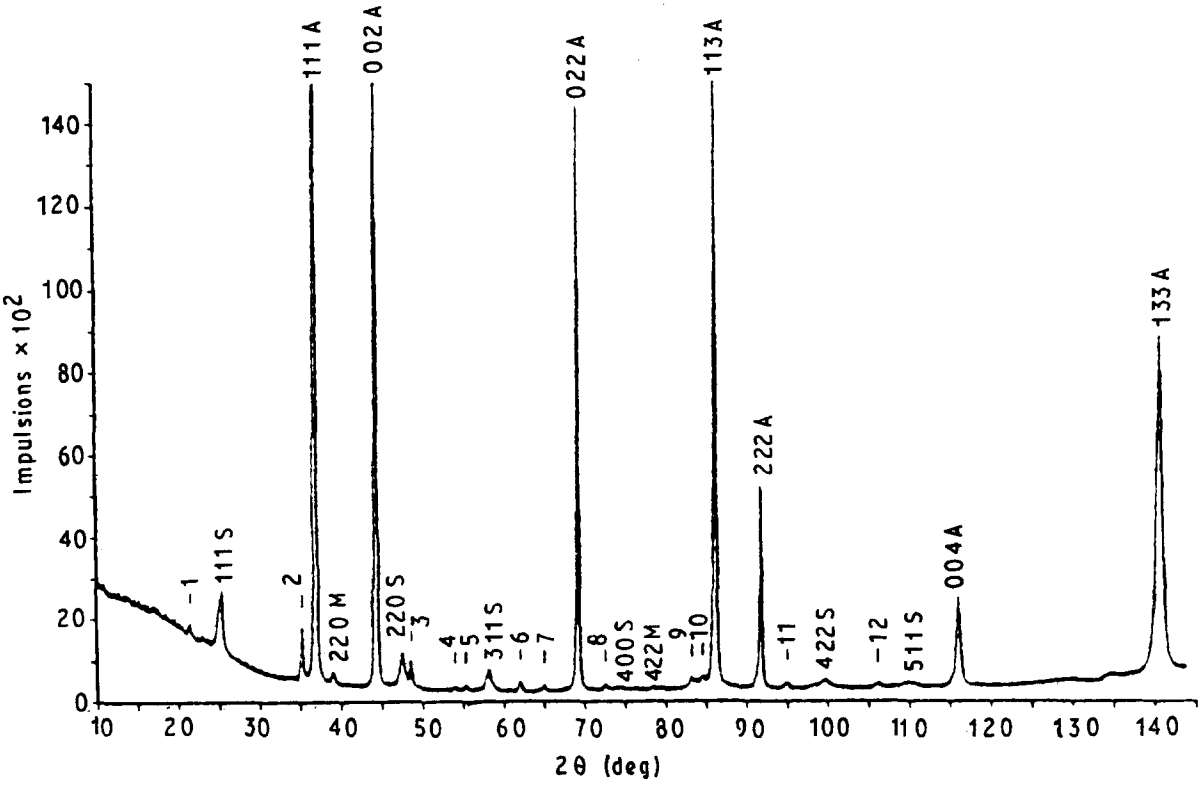

Figure 12 X-ray diffraction pattern obtained from as-melt quenched Al–Si–Mg powders.

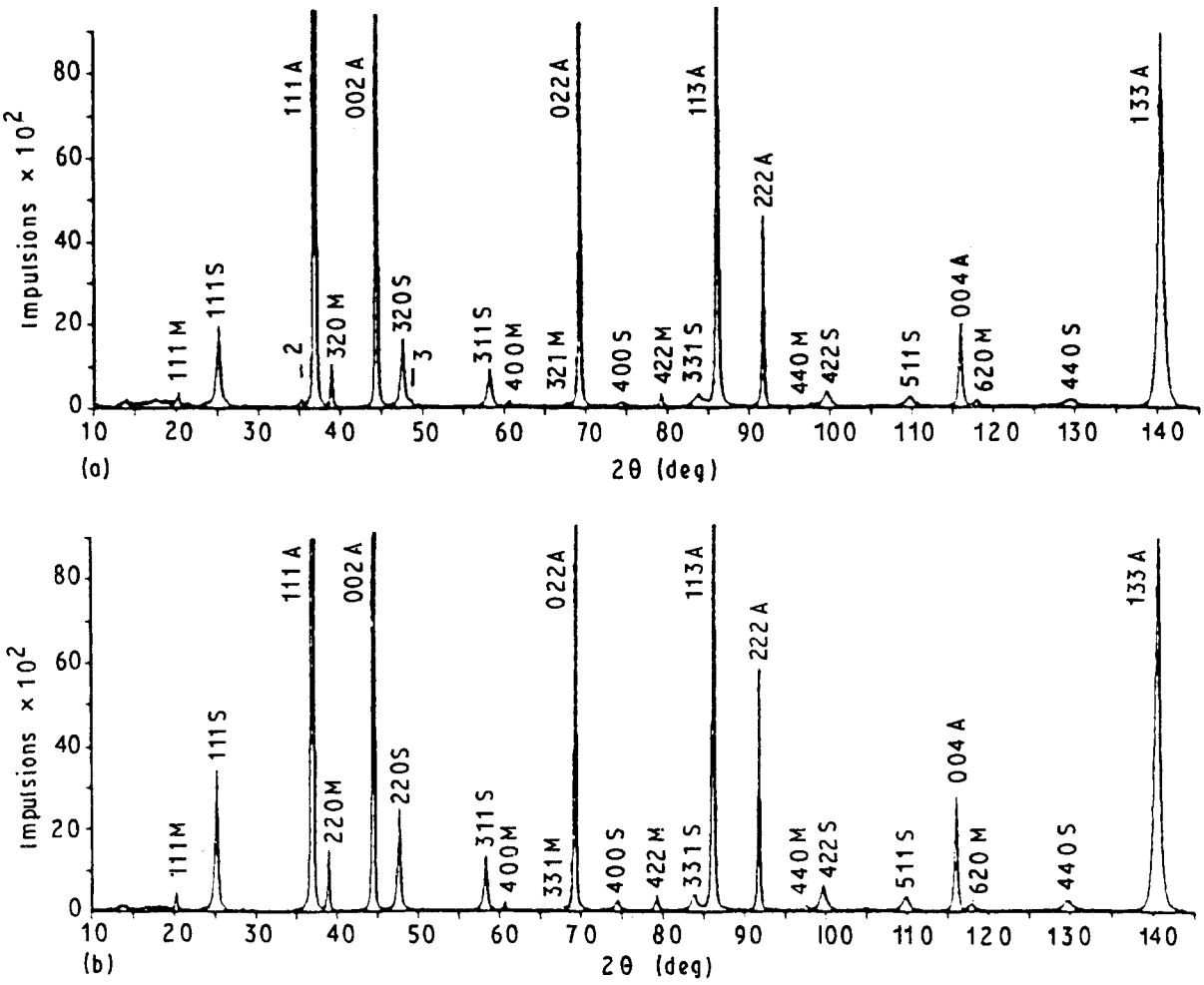

Figure 13 X-ray diffraction patterns obtained from Al–Si–Mg powders after ageing 24 h at: (a) 200 and (b) 250 °C.

TABLE VI Position of peaks characteristic of the meta-stable phase in Al–Si–Mg alloys

Peak number	1	2	3	4	5	6	7	8	9	10	11	12
2θ (deg)	29.37	43.24	56.60	61.98	63.34	70.05	73.03	80.61	91.27	92.60	103.0	114.2
d (nm)	0.3528	0.2478	0.1887	0.1737	0.1703	0.1558	0.1503	0.1383	0.1251	0.1237	0.1143	0.1065
q (nm^{-1})	0.1781	0.2588	0.3330	0.3617	0.3689	0.4033	0.4180	0.4543	0.5023	0.5079	0.5497	0.5900

2. Coarse microstructure of equiaxed dendrites of α-Al. This microstructure was very close to that viewed from the gas side, Fig. 3a.

From these micrographs and others, some thermal parameters could be calculated and are listed in Table VII. These calculations are based on the assumption that there is only one nucleation event and the ratio of the external surface (S^*) to the solid/liquid interface surface (S) is unity.

The variation in the microstructural details, even in the interior of the same powder particle is explicable in terms of:

(a) The existence of two solidification mechanisms, first adiabatic (high interface velocity and recalescence), then isothermal (progress of the interface controlled by the external flux).

(b) The variation in the S^*/S ratio.

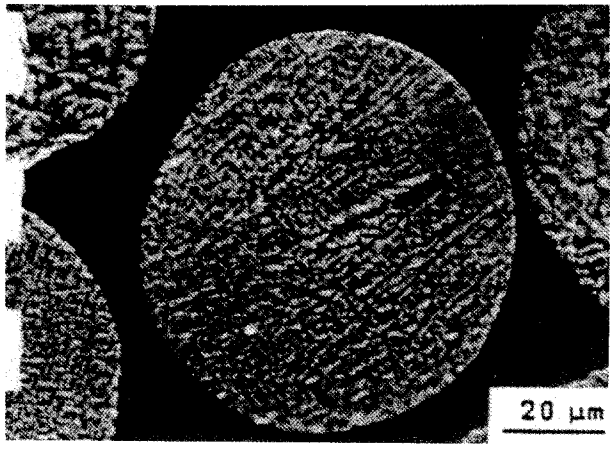

Figure 14 Optical microstructures of loose powders of Al–12% Si alloy with different particle sizes.

TABLE VII Thermal parameters calculated from the microstructure of powder particles with different sizes

d(μm)	25	50	80	100	125	200
H (10^4 Wm^2K^{-1})	2.4	1.5	1.0	0.9	0.8	0.6
R_{min} (10^{-3} ms^{-1})	12.4	7.7	5.2	4.6	4.1	3.1
$\dot{T}$ (10^5 Ks^{-1})	11.00	3.40	1.40	1.00	0.72	0.34
Calculated SDAS (μm)	0.46	0.67	0.90	1.00	1.10	1.50
Measured SDAS (μm)	0.5–0.9	0.6–1.0	0.8–1.1	0.8–1.5	1.0–1.7	1.1–1.7

Calculations made [21] show that the first explanation is correct.

Thin foils were prepared from loose powders with diameters in the range 25–50 μm. It seems that intercellular or interdendritic materials contain Si particles that are either in the form of elongated needles (Fig. 15a, 2 μm long and 0.2 μm thick) or else spherical (with diameters in the range of 0.15–0.35 μm, Fig. 15b). For Al–Si–Sr powders, the Si particles were always spherical, with diameters ranging between 50–100 nm, Fig. 16.

TEM examination of extruded powders allows for more precise measurements of α-grain, and Si particle size, Fig. 17. About 400 silicon particles over a surface of 5.8×10^{-11} μm^2 were measured. Taking the thickness of the thin foil to be about 0.7 μm, a volumetric number, N_v, of the order of 7×10^{19} m^{-3} is obtained, that represents a volume fraction, f_v, of about 0.136. Assuming all Si particles are spherical, their average diameter can be calculated as follows

$$d = \left[\frac{6f_v}{\pi N_v}\right]^{1/3} = 160 \text{ nm}$$

Specimens from extruded Al-12% Si were aged at 200, 300 and 400 °C for times up to 10 h. Optical examination did not reveal noticeable microstructural changes on ageing at 300 °C. After 2 h at 400 °C, crystals of silicon up to 2 μm could be measured. After 10 h at this temperature, the size of the Si particles was about 4 μm. At 500 °C, their respective diameters were 4 and 8 μm.

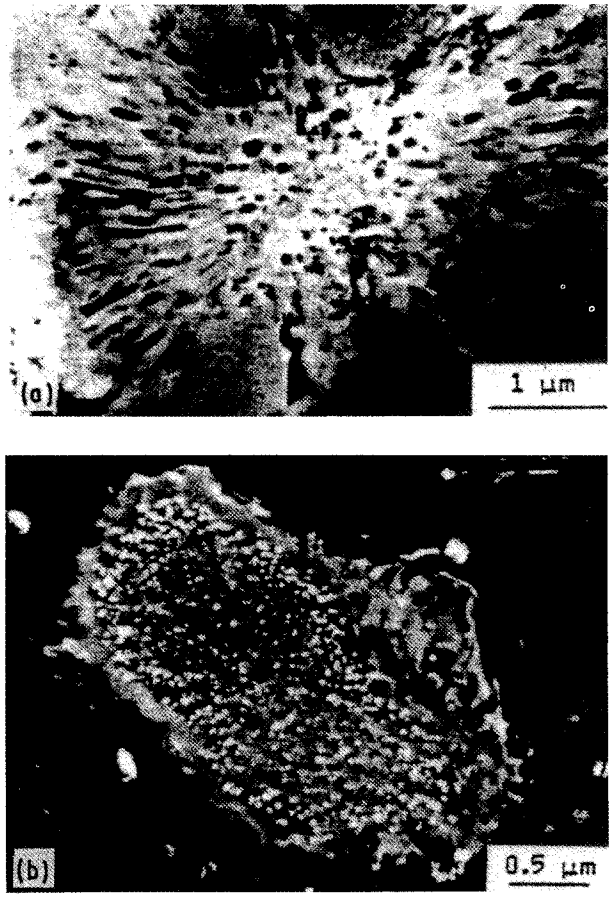

Figure 15 TEM micrographs corresponding to Al–12% Si loose powders, showing (a) elongated Si particles, bright field and (b) spherical Si particles, dark field.

3.2.3. Mechanical properties

The tensile properties of as-extruded Al–Si–x powders compared to ingot metallurgy (IM) are summarized in Table VIII. The properties of binary Al-12% Si alloy are markedly improved by rapid solidification; $\sigma_{0.2}$ = 100%, σ_E = 60%, EL = 100%, R.A. = 400%. The yield strength as well as ultimate tensile strength are further improved by the addition of Cu, Ni and Mg as ternary elements. This is accompanied by a noticeable reduction in alloy ductility. Addition of Co leads to a significant improvement in all the three parameters.

Table IX gives the tensile results obtained after ageing the extruded Al–12% Si powders at 200, 300, 400 and 500 °C, for times up to 10 h. After 10 h at 200 and 300 °C, not much change could be observed in the elastic limit and ultimate tensile strength values, whereas the ductility increased from 19 to 24%. At 400

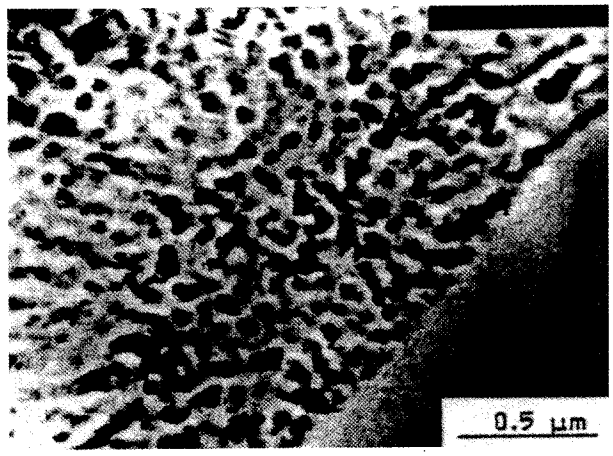

Figure 16 Bright field micrograph corresponding to Al–Si–Sr loose power.

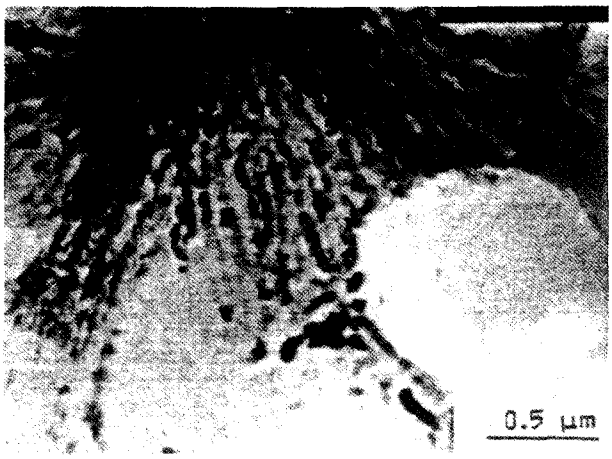

Figure 17 Bright field micrograph of as-extruded Al–12% Si powders.

and 500 °C, a significant reduction in both $\sigma_{0.2}$ and σ_E was obtained, with an increase in alloy ductility that reached 31% at 500 °C.

The extruded rods were heat treated as follows:

1. Ageing for 12 h at 170 °C.
2. Solution heat treatment 0.5 h at 500 °C, followed by quenching in water at 20 °C.
3. Treatment 2 plus ageing for either 6 h at 170 °C (Al–Si–Cu alloy) or 8 h at 160 °C (Al–Si–Mg alloy).
4. Same as Treatment 3 except 2 h solution heat treatment instead of 0.5 h.

TABLE VIII Mechanical properties of as-extruded powders $\sigma_E = F_{max}/S_0$, $\sigma_R = F_{max}/S_{rupture}$, EL = $\Delta L/L_0$ and R.A. = $\Delta A/A_0$.

Alloy	$\sigma_{0.2}$ (MPa)	σ_E (MPa)	σ_R (MPa)	EL (%)	R.A. (%)
Al–12% Si	162	244	324	19	47
Al–Si–Cu	223	386	435	7	14
Al–Si–Mg	233	296	381	15	41
Al–Si–Ni	253	333	384	13	27
Al–Si–Co	207	254	371	20	68
Al–Si–Sr	197	283	345	18	51
Al–Si (IM)	79	185	202	9	9

Typical stress-strain curves obtained from 3 sets of tests of as-extruded materials are shown in Fig. 18a–d. The results obtained after heat treatment are summarized in Table X. It is evident from this that a strong light alloy of type Al–12% Si could be produced with a minimum ductility of 5%.

The present results are compared with those reported in the literature in Table XI. Apparently, using the centrifugal atomization process to produce powders leads to improved mechanical properties after extrusion as compared to those produced employing the gas atomization process [22, 23]. Yamauchi [24], could obtain, for the same Al–12% Si alloy, higher strength with lower ductility values. From his results, superior mechanical properties are attainable from hyper-eutectic water atomized alloys, in contrast to those associated with alloys produced by ingot metallurgy. Attempts were made by Van Rooijen *et al.* [25] to produce solid bars from broken ribbons through hot extrusion at relatively high temperatures, 450–460 °C. For Al–12% Si, they reported a UTS value of 165 MPa which is almost half the value listed in Table XI for the present alloy.

Fig. 19a represents the fractograph of as-extruded Al–12% Si alloy, comprising of equiaxed fine dimples with an average diameter of less than 2.5 cm. In the case of alloys made by ingot metallurgy, the dimples were mostly elongated with dimensions around 2 μm × 10 μm. The difference in the morphology and dimple size is strongly related to the form and size of the eutectic Si. Fig. 19b shows the presence of porosity. These pores are mainly due to insufficient degassing and lead to a certain incoherency at the grain boundaries.

4. Conclusions

1. The solidification process of melt-spun ribbons takes place in three stages:

(a) Nucleation of α-phase in a liquid with a strong undercooling.
(b) Adiabatic solidification and recalescence during which the liquid/solid interface moves from the wheel side towards the gas side.

TABLE IX Mechanical properties of extruded Al–12% Si powders, aged at 200, 300, 400 and 500 °C for various times

Ageing temperature (°C)	Ageing time (h)	Property		
		$\sigma_{0.2}$ (MPa)	σ_E (MPa)	EL (%)
200	2	–	–	–
	4	–	–	–
	10	169	237	22
300	2	151	218	23
	4	153	219	24
	10	158	216	24
400	2	134	202	25
	4	128	193	26
	10	123	186	27
500	2	105	173	29
	4	74	158	30
	10	74	156	31

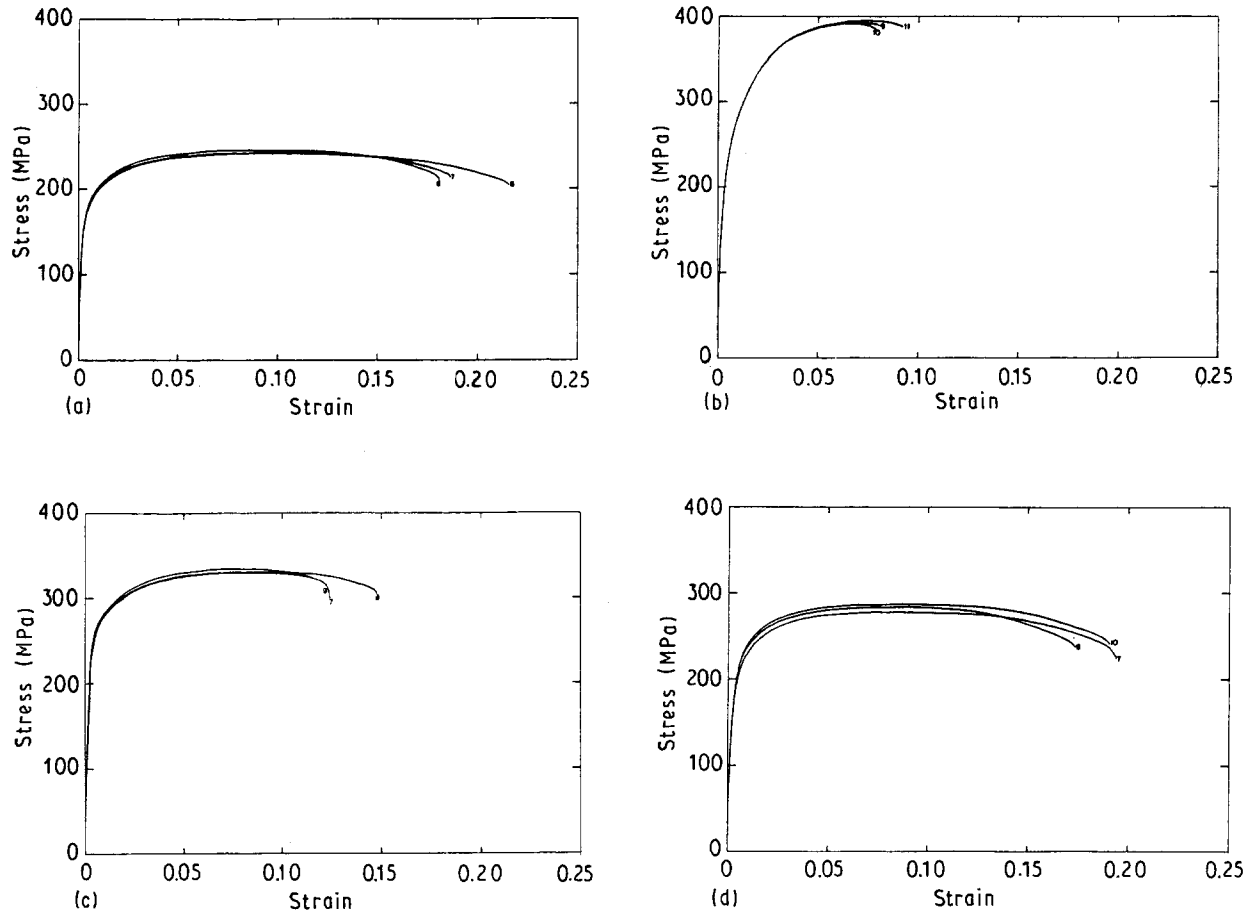

Figure 18 Typical stress-strain curves for as-extruded: (a) Al–12% Si; (b) Al–12% Si–4.6% Cu; (c) Al–12% Si–2.1% Ni and (d) Al–12% Si–0.5% Sr.

TABLE X Mechanical properties of heat treated Al–Si–x hot extruded alloys

Alloy	Heat treatment	$\sigma_{0.2}$ (MPa)	σ_E (MPa)	EL (%)
Al–Si–Cu	As-extruded	223	386	7
	1	235	400	9
	2	250	450	8
	3	363	476	5
Al–Si–Mg	As-extruded	233	296	15
	1	216	294	16
	2	270	370	12
	3	380	425	5
	4	370	405	6
Al–Si–Ni	As-extruded	253	384	13
	1	238	332	14

(c) Nucleation and growth of α-phase in liquid in front of the moving interface.

2. Undercooling and interface velocity are maximum at the beginning of stage (b) in 1. Solute atoms will be trapped in the solid part due to the weak diffusion rate in the liquid state. This process leads to solid material supersaturated in Si, which is unstable and decomposes during cooling, giving rise to fine particles distributed in a uniform manner and maintaining an orientation relationship with the matrix. This structure is known as a non-segregated structure.

3. For the atomized powders, solidification occurs by heterogeneous nucleation at the interface with the atmosphere (helium) followed by propagation of the solidification front towards the particle centre. In this

TABLE XI Comparison of the present results with those reported in literature

Reference	Alloy	Pulverization	Extrusion temperature (°C)	σ_E (MPa)	EL (%)
[21]	Al–14Si–4Cu–1Mg–4Ni (age hardened)	Gas	500	482	2
[22]	Al–17Si–4Cu (age hardened)	–	–	346	2
[23]	Al–12Si	Water	320	275	10
	Al–17Si	Water	320	326	9
Present work	Al–12Si	Centrifugal	250	244	19
	Al–12Si–4.6Cu (age hardened)	Centrifugal	250	476	5

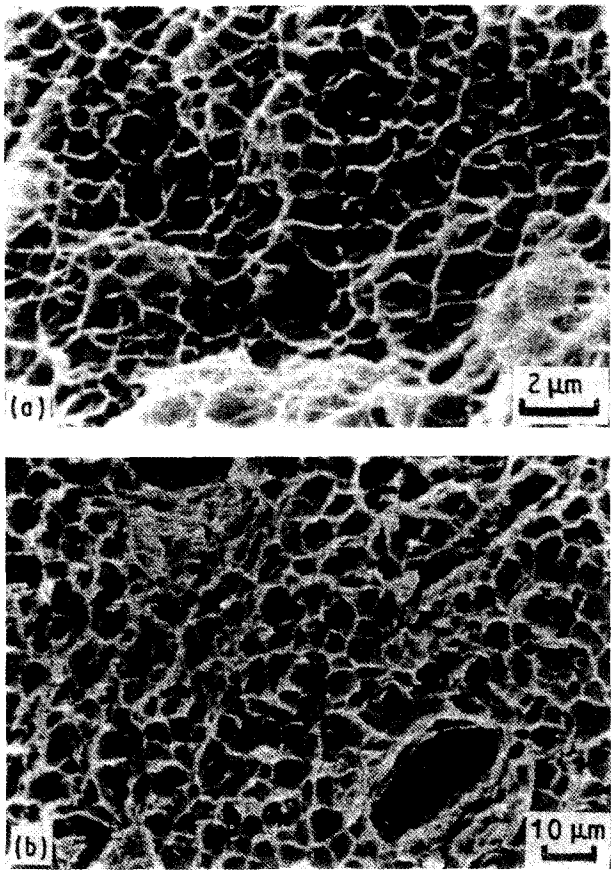

Figure 19 Tensile fracture surface of Al–12% Si alloy (a) as-extruded (b) aged 10 h at 500 °C.

case and under similar conditions of liquid cooling equivalent to those reported for melt-spun ribbon, we did not observe sufficient undercooling that resulted in a non-segregated solid structure.

4. Up to 20% Si for melt spinning and 12% Si for centrifugally atomized powders, the structure is hypo-eutectic.

5. For binary Al–12% Si alloys, tensile properties of hot extruded powders are much improved compared to those obtained from alloys made by ingot metallurgy. For ternary alloys, the materials exhibit a structural hardening with a noticeable loss in ductility after solid solution treatment.

References

1. F. H. SAMUEL, *Metall. Trans.* in Proceedings of the Third **17A** (1986) 73.
2. G. CHAMPIER and F. H. SAMUEL, International Conference on Al–Li Alloys, University of Oxford, England, 1986, (Institute of Metals, London, 1986) p. 131.
3. F. H. SAMUEL, *Metall. Trans.* **17A** (1986) 127.
4. F. H. SAMUEL and G. CHAMPIER, *J. Mater. Sci.* **23** (1988) 541.
5. F. H. SAMUEL, A. M. SAMUEL and G. CHAMPIER, in "Production Refining, Fabrication and Recycling of Light Metals", edited by M. Bouchard and P. Tremblay (Pergamon, 1990) p. 241.
6. T. F. KELLY and F. B. VAN DER SANDE, in "Rapid Solidification Processing Principles and Technologies II" (Claitors Publishing Division, Baton Rouge, 1980) p. 100.
7. A. K. KUSHNEREVA and I. V. SAILLI, *Inorg. Mater.* **6** (1970) 1644.
8. K. F. KOBAYASHI, M. KUMIKAVA and H. SHINGU, *J. Jpn. Inst. Metals* **49** (1985) 1.
9. E. J. MITTEMEIJER, P. VAN MOURIK and T. H. DE KEIJER, *Phil. Mag.* **43** (1981) 1157.
10. E. OZAWA and H. KIMURA, *Mater. Sci. Eng.* **8** (1971) 327.
11. G. R. ARMSTRONG and H. JONES, "Solidification and Casting of Metals" (Metals Society, London, 1979).
12. H. MATYJA, B. C. GIESSEN and N. J. GRANT, *J. Inst. Metals* **96** (1968) 30.
13. T. W.CLYNE, *Metall. Trans.* **15B** (1984) 369.
14. W. W. MULLINS and R. F. SEKERKA, *J. Appl. Phys.* **35** (1964) 444.
15. S. R. CORIELL and R. F. SEKERKA, "Rapid Solidification Processing Principles and Technologies II" (Claitors Publishing Division, Baton Rouge, 1980) p. 35.
16. M. J. AZIZ, *J. Appl. Phys.* **53** (1982) 2.
17. V. N. GUDZENKO and A. F. POLESYA, *Izvest V.U.Z. Tsvetnaya Met.* **4** (1973) 144.
18. B. PREDEL and K. HULSE, *Z. Metallkunde* **69** (1978) 691.
19. C. SURYANARAYANA, S. TIWARI and T. R. ANANTHARAMAN, *ibid.* **3** 155.
20. P. COULOMB, " Les textures dans les métaux de réseau cubique" (Dunod, Paris, 1972).
21. C. C. LEVI and R. MEHRABIAN, *Metall. Trans.* **13A** (1982) 13, 221.
22. C. PANSERI and M. PAGANELLI, in Proceedings of the European Symposium on Powder Metallurgy, Stuttgart, Vol. III, 1968.
23. R. PERROT, *Revue de l'aluminum* (1979) p. 129.
24. I. YAMAUCHI, I. OHNAKA, S. KAWAMOTO and T. FUKUSAKO, *J. Jpn Inst. Metal*, **49** (1985) 231.
25. VAN ROOIJEN, J. A. VAN DER HOEVEN, L. KATGERMAN, P. VAN MOURIK, T. H. DE KEIJER and E. J. MITTEMEIJER in Proceedings of the Conference on PM Aerospace Materials, Bern, 12–14 November 1984.

Received 22 February
and accepted 13 May 1991